Arabian Journal of Chemistry (2023) **16**, 104624

King Saud University

Arabian Journal of Chemistry

www.ksu.edu.sa
www.sciencedirect.com

ORIGINAL ARTICLE

Constructing recyclable photocatalytic BiOBr/Ag nanowires/cotton fabric for efficient dye degradation under visible light

Lili Wang [a], **Xiaohui Ren** [a], **Lei Chen** [a], **Haiyan Mao** [a], **Dawei Gao** [a,*], **Yuyang Zhou** [b,*]

[a] *College of Textiles and Clothes, Yancheng Institute of Technology, Yancheng 224051, China*
[b] *National Engineering Laboratory for Modern Silk, College of Textile and Clothing Engineering, Soochow University, Suzhou 215123, China*

Received 16 November 2022; accepted 22 January 2023
Available online 25 January 2023

KEYWORDS

BiOBr;
Ag nanowires;
Photodegradation;
Reusable photocatalyst;
Visible-light degradation

Abstract In this study, a highly-efficient photocatalytic and recyclable BiOBr/Ag nanowires (AgNW)/cotton fabric (CF) composite was fabricated by successive ionic layer adsorption and reaction (SILAR) for rapid treatment of dye wastewater. The integration of AgNW and BiOBr aims to establish a channel for faster and easier charge transfer to enhance the photocatalytic performance. The chemical structure and morphology of BiOBr/AgNW/CF, as well as its photo-degradation of Rhodamine B (RhB) under visible light radiation were explored. Results reveal that BiOBr/AgNW/CF exhibits remarkably enhanced photocatalytic activity over BiOBr/CF, which degrades 97 % of RhB within 90 min. BiOBr/AgNW/CF still maintains 88 % of photocatalytic degradation capacity after five reusing cycles due to the effective encapsulation of BiOBr that protects AgNW from oxidation. Photoluminescence, electron spin resonance, and free radical trapping experiments confirm that the separation efficiency of photo-generated electron-hole pairs plays an important role in improving photocatalytic performance. In all, this work exhibits great potential in the development of textile-based photocatalytic materials that integrates two significant merits, the high degradation efficiency and easy recovery.

---

* Corresponding authors.
E-mail addresses: gaodawei@ycit.edu.cn (D. Gao), yuyang_suda@hotmail.com, yuyangzhou@suda.edu.cn (Y. Zhou).

Peer review under responsibility of King Saud University.

ELSEVIER **Production and hosting by Elsevier**

https://doi.org/10.1016/j.arabjc.2023.104624

1. Introduction

With increasing demand for diverse textile products from customers, the discharge of wastewater during textiles' dyeing and finishing, is an intensifying issue that endangers human health and the environment. Every year, textile enterprises consume about 70,000 tons of dyes, and 40 % of which causes pollution. Textile dye wastewater accounts for 17–20 % of the total industrial wastewater, which induces non-ignorable environmental pollution without proper subsequent treatment (Liu et al., 2021; Uddin, 2021; Slama et al., 2021). Hence, dyes are required to be decolorized and removed from wastewater before discharging (Tkaczyk et al., 2020).

Conventional dye wastewater treatment involves physical, chemical, or biological techniques, however most of them still show various disadvantages including the incomplete removal of organic pollutants, the complexity of the treatment process, the high cost, and potential generation of secondary pollution (Piaskowski et al., 2018; Ishak et al., 2020; Bustos-Terrones et al., 2021). For example, the physical removal of dyes and other organic pollutants, is an intrinsic phase transferring process rather than dye decomposition, which results in another kind of pollution (Li et al., 2019; Srivatsav et al., 2020). Chemical oxidation is only beneficial to the removal of high concentration pollutants economically, however could hardly eliminate dyes completely (Yang et al., 2021). The disadvantages of biological treatment are related to the slow reaction rate, sludge disposal, and the requirement of controllable pH value and temperature (Bhatia et al., 2017; Meerbergen et al., 2017). It is found that the photocatalytic technology based on semiconductors own several advantages such as simple operation, mild reaction conditions, high efficiency, environmental protection, and wide applicability. Therefore, photocatalytic technology is promising in handling the issue of organic pollutants (Akhundi et al., 2019, 2020, 2022).

In addition, the key objective of photocatalytic technology is to develop efficient photocatalysts. A large number of powder-shaped semiconductor nanomaterials have been developed as the most widely used and effective photocatalysts, such as TiO_2 (Chairungsri et al., 2022; Sabri et al., 2021) and ZnO (Chimupala et al., 2020). However, these powered photocatalysts are merely excited by UV light, which severely hinders their practical application, especially for the treatment of flowing wastewater. Fortunately, fabric-based catalyst is a promising functional composite material that combines the advantage of reusability and cost-effectiveness compared with conventional powder-like photocatalysts (Xu and Ma, 2021). Cotton fabric is an appropriate support substrate for micro/nanomaterials due to its abundance, renewability, and biodegradability (Noureen et al., 2020). To solve this problem, we would use cotton fabric (CF) as a flexible porous substrate to prepare novel filter-like photocatalysts, which are easy to recycle and degrade organic dyes in flowing wastewater. Moreover, using CF to load and disperse photocatalysts can effectively prevent the photocatalysts from agglomeration and improve their photocatalytic performance.

Nowadays, bismuth oxyhalides (BiOX, X = Cl, Br, and I) have attracted much attention due to their unique structure and electrical properties (Li et al., 2021; Yang et al., 2018). Among them, BiOBr (band gap ~2.8 eV) has attracted attention in the application of photocatalysis because of its unique tetragonal martensite structure with $[Bi_2O_2]^{2+}$ sections interspersed with the dibromide layers (Shi et al., 2019, 2020). However, the rapid recombination of photogenerated electrons and holes greatly hinders the activity and application of BiOBr photocatalysts. So far, the strategies to improve the photocatalytic performance of BiOBr include morphology control, semiconductor compounding, and noble metal deposition, etc. (Geng et al., 2017; Guo et al., 2019; Wu et al., 2016). Silver (Ag) has excellent electrical properties and promotes the transfer of photogenerated electrons (Hou et al., 2017; Li et al., 2021). Thus, Ag is an efficient but low-cost material to readily integrate with BiOBr. However, the effect of Ag oxidation on the catalytic performance is insufficient. Because, once Ag is oxidized, the photocatalytic performance of the Ag-containing catalysts is reduced (Gao et al., 2019). Therefore, the retention of Ag is of great significance to improve photocatalytic performance. Besides, the surface coating of BiOBr enables effective protection of Ag from oxidation or corrosion, which ensures the chemical stability of the hybrid nanostructure of the photocatalyst.

In this work, the BiOBr/AgNW/CF photocatalytic composite was successfully synthesized by a simple impregnation process and successive ionic layer adsorption and reaction (SILAR) methods (Fig. 1). The structure and morphology of the BiOBr/AgNW/CF was studied systematically. The photocatalytic performance and mechanism under visible light irradiation was also investigated, which provides a simple, novel and pollution-free way for designing and preparing stable photocatalytic degradation in dye wastewater treatment.

2. Experimental section

2.1. Materials

The cotton fabric (CF) (40×60 mm^2) was obtained from Yancheng Kaiyuan Textile Co., Ltd. (China). And the cotton fabric was washed three times alternately with ethanol and water, then dried at 60 ℃ for 1 h. Silver nitrate ($AgNO_3$), polyvinylpyrrolidone (PVP), bismuth nitrate pentahydrate ($Bi(NO_3)_3$■$5H_2O$) and potassium bromide (KBr) were bought from Sigma Aldrich (China). Rhodamine B (Rh B), sodium chloride (NaCl), ethylene glycol (EG) and anhydrous ethanol were acquired from Sinopharm Chemical Regent Co., Ltd. All chemicals were directly used without purification and were analytical grade. The water used in the experiment is deionized water.

2.2. Synthesis of AgNW

Ag nanowires (AgNW) was synthesized based on the polyol method (Weng et al., 2019; Zhu et al., 2022). PVP (350 mg) was dissolved in ethylene glycol (EG, 20 mL) under magnetic stirring. NaCl (6 mg) was added to the solution. After the NaCl was dissolved, the $AgNO_3$ solution (100 mg, 10 mL EG) was added to the mixture and stirred for 1 min. Transfer the mixture to the reactor and heated it at 160 ℃ for 3 h. After cooling to the room temperature, the mixture was centrifuged at 2000 rpm (3 times, 5 min each time). Finally, the obtained AgNW was dispersed in ethanol for subsequent experiments.

2.3. Preparation of conductive cotton fabric

The conductive cotton fabric was prepared through a simple impregnation method (Fig. 1). AgNW was dispersed in ethanol to 0.5 mg/mL, and then pure cotton fabric (40×60 mm^2) was repeatedly impregnated in the prepared AgNW solution, in which the impregnation time was 5 s and the drying temperature was 50 ℃. After 10 times of the above cycle, the conductive cotton fabric AgNW/CF was obtained.

2.4. Fabrication of BiOBr/AgNW/CF composites

The BiOBr/AgNW/CF composites were prepared via the SILAR method shown in Fig. 1 (Ratnayake et al., 2021). Specifically, $Bi(NO_3)_3$ (1.5 g) and KBr (0.35 g) were initially dissolved separately in 500 mL of ultrapure water. AgNW/

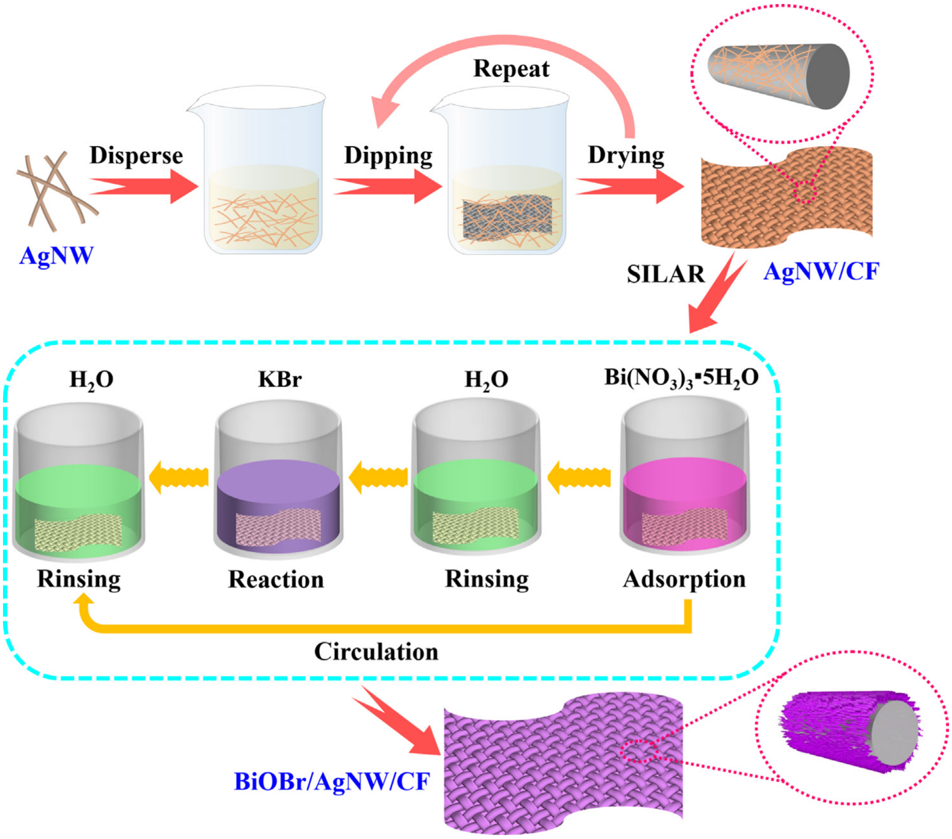

Fig. 1 Scheme for the fabrication of BiOBr/AgNW/CF composites.

CF was immersed into 6 mM of $Bi(NO_3)_3$ solution for 1 min, and washed with deionized water. Then the sample was immersed into 6 mM of KBr solution for 1 min, and washed with deionized water. The above immersing progress was named as one SILAR cycle. After a series of cycles, the samples were thoroughly washed with deionized water and dried at 55 ℃ in a vacuum oven for 6 h. The BiOBr/AgNW/CF samples prepared with SILAR circulations of 3, 6, 9 and 12, were labeled as 3BiOBr/AgNW/CF, 6BiOBr/AgNW/CF, 9BiOBr/AgNW/CF and 12BiOBr/AgNW/CF, respectively. For comparison, raw cotton fabric treated with 9 cycles was also prepared and denoted as 9BiOBr/CF.

2.5. Characterization

The X-ray diffraction (XRD) patterns of samples were recorded via an X-ray diffractometer (MAC Science Co. Ltd. MXP 18 AHF, CuKα) at 2θ angles ranging from 10° to 80°. Morphologies of the prepared samples were taken on the scanning electron microscope (FESEM, JOEL, JSM-6700F). Meanwhile, the energy dispersive X-ray spectroscopy (EDS, X-Max, Oxford Instruments) attached to the SEM was used to verify the components of BiOBr/AgNW/CF composites. The surface chemical composition of BiOBr/AgNW/CF composites was analyzed by X-ray photoelectron spectroscopy (XPS, PHI Quantum 2000). The UV–vis reflectance spectra were recorded on PerkinElmer Lambda UV–vis-NIR spectrometer. The photoluminescence (PL) property was obtained over Varian Cary Eclipse spectrometer. The decomposition degree was evaluated by the total organic carbon analyzer (TOC-VCPH, Shimadzu). The active species were confirmed by the radical capture and electron spin resonance (ESR, JEOL, JES-TE200).

2.6. Photocatalytic study

The photocatalytic activity of samples was evaluated by degrading RhB under visible light illumination (Wang et al., 2023). The sample was immersed in 60 mL RhB solution with concentration of 10 mg/L, and stored at least 30 min in the dark to achieve the adsorption–desorption equilibrium. Then, 2 mL solution was sampled every 10 min under 500 W xenon light irradiation, and the absorbance of the solution was measured by a Hitachi UV-1080 spectrophotometer, in which, the maximum absorbance wavelength of RhB is about 552 nm (Fig. S1). The photodegradation rate was defined as C/C_0, in which C_0 was the initial concentration of RhB after equilibrium and C was the concentration at different time intervals after irradiation. In addition, to evaluate the stability of the photocatalytic composite material, the sample was recycled 5 runs after each experiment by washing and drying. The photocatalytic mechanism of BiOBr/AgNW/CF was explored through radical scavenging experiments in the presence of radical scavengers. Three separate solutions containing EDTA-2Na (1 mL), BQ (1 mL), and *t*-BuOH (1 mL) were added into three identical RhB solutions to capture h^+, $\cdot O_2^-$ and $\cdot OH$ respectively, and subject to sunlight irradiation.

3. Results and discussion

3.1. Structural characterization

3.1.1. XRD analysis

The XRD patterns of AgNW, AgNW/CF, 9BiOBr/CF, 3BiOBr/AgNW/CF, 6BiOBr/AgNW/CF, 9BiOBr/AgNW/CF and 12BiOBr/AgNW/CF are shown in Fig. 2a. For cotton fabric, the characteristic peaks at 15.12°, 16.61°, and 22.74° corresponds to the respective (1−10), (1 1 0), and (2 0 0) peaks of the cellulose I_β pattern (Wang et al., 2018; Zhang et al., 2014). When the cotton fiber is covered by large quantity of AgNW, two characteristic peaks appeared at 38.17° and 44.31° are observed, which represent the (1 1 1) and (2 0 0) crystal planes of the face-centered cubic structure of metallic Ag, respectively (Cheon et al., 2018). For 9BiOBr/CF, six diffraction peaks are observed at 32.27°, 34.05°, 46.24°, 57.21°, 67.42° and 77.08°, which correspond to the (1 1 0), (1 1 1), (2 0 0), (2 1 2), (2 2 0) and (3 1 1) crystal planes of tetragonal phase BiOBr, respectively (Lv et al., 2020). Upon the increase of SILAR cycles, the characteristic peak of BiOBr show an enhanced trend in intensity. In all BiOBr/AgNW/CF composites, the lattice structure of BiOBr is not affected by the AgNW. The formation of BiOBr/AgNW/CF composite is further proved by TEM image with high resolution (Fig. 2b). The observed lattice fringe spacing of 0.196 nm matches with the (1 1 0) crystal plane of BiOBr (Yu et al., 2020). The lattice fringe spacing measured to be 0.24 nm corresponds to the (1 1 1) crystal plane of metal AgNW (Celebioglu et al., 2019). Combined with the XRD patterns, it is confirmed that the heterostructures between BiOBr and AgNW are successfully prepared on the CF.

3.1.2. SEM-EDS analysis

As seen in Fig. 3a, a large number of AgNW intersect with each other, making the cotton fibers partially covered or wrapped. Furthermore, the AgNW are wholly exposed to the air. The morphology of 9BiOBr/CF is shown in Fig. 3b. The cotton fabric is utterly covered and wrapped by BiOBr nanosheets. In Fig. 3(c–f), AgNW/CF is also covered and wrapped by BiOBr, and the structure of AgNW resembles shape of line. With the increase of the number of SILAR, large quantity of AgNW are embedded in the cotton fiber and protected by BiOBr. Only a small amount of them is exposed to the air. After 9 SILAR circles, the AgNW/CF surface is almost entirely covered by BiOBr nanosheets. A further increase in the number of SILAR cycles led to accumulation of BiOBr nanosheets on the surface. Thus, the nanostructure, and coverage density of BiOBr/AgNW/CF are able to be manipulated by adjusting the SILAR cycles, which further influence the catalytic activity and the reusability of the final product. It is also worth noting that excessive deposition of BiOBr on AgNW/CF is not conducive to the improvement of photocatalytic performance, which is further confirmed in the following Section 3.2.3. *Photocatalytic degradation performance*.

To explore the elemental composition of 9BiOBr/AgNW/CF, EDS analysis was conducted. The EDS spectrum mappings (Fig. 4) indicate that Ag, Bi, Br, O and C element are homogeneously distributedthroughout the whole sample, which also confirms the successful incorporation of AgNW and BiOBr onto the cotton fabric surface.

3.1.3. XPS analysis

The chemical compositions and valence states of 9BiOBr/AgNW/CF were studied by XPS. As shown in Fig. 5a, the survey spectra of 9BiOBr/AgNW/CF show the presence of Ag, Bi, Br, O and C elements. Such result is consistent with the findings from EDS. The peaks at 367.6 eV and 373.7 eV are attributed to Ag 3d (Fig. 5b) (Weng et al., 2019). For the Bi element, the Bi 4f orbitals are detected, so in their corresponding maps, 159.4 eV and 164.7 eV correspond to Bi $4f_{7/2}$ and Bi $4f_{5/2}$, respectively, indicating that Bi existed in the form of Bi^{+3} (Ling et al., 2020; Miao et al., 2018). In the energy spectrum of the Br element (Fig. 5c, d), the characteristic peaks at 68.5 eV and 69.5 eV belonged to Br $3d_{5/2}$ and Br $3d_{3/2}$, respectively, indicating that Br existed in the form of Br^- in the sample (Wang et al., 2014). After fitting, the O 1 s orbit was confirmed to be the three characteristic peaks of 530.2 eV, 531.4 eV and 532.5 eV (Fig. 5e). The apparent characteristic peak of 530.3 eV (Bi—O) corresponds to the lattice oxygen of the composite. The characteristic peak of 531.4 eV is generated by oxygen vacancy. The characteristic peak of 532.3 eV is related to the hydroxyl or water adsorbed on the surface of the

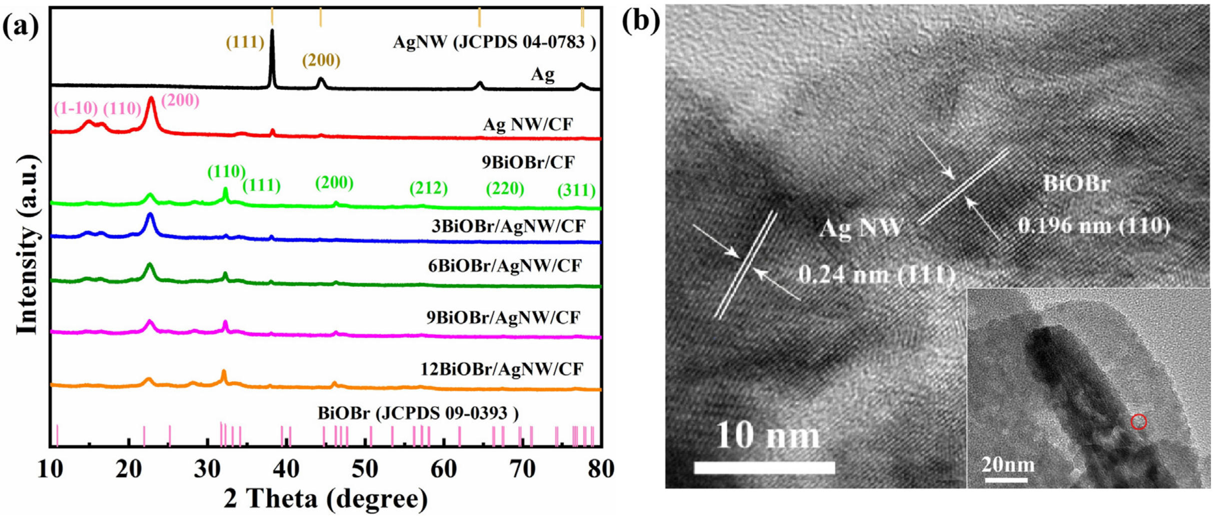

Fig. 2 (a) XRD patterns of the composites, (b) TEM and HRTEM images of BiOBr/AgNW.

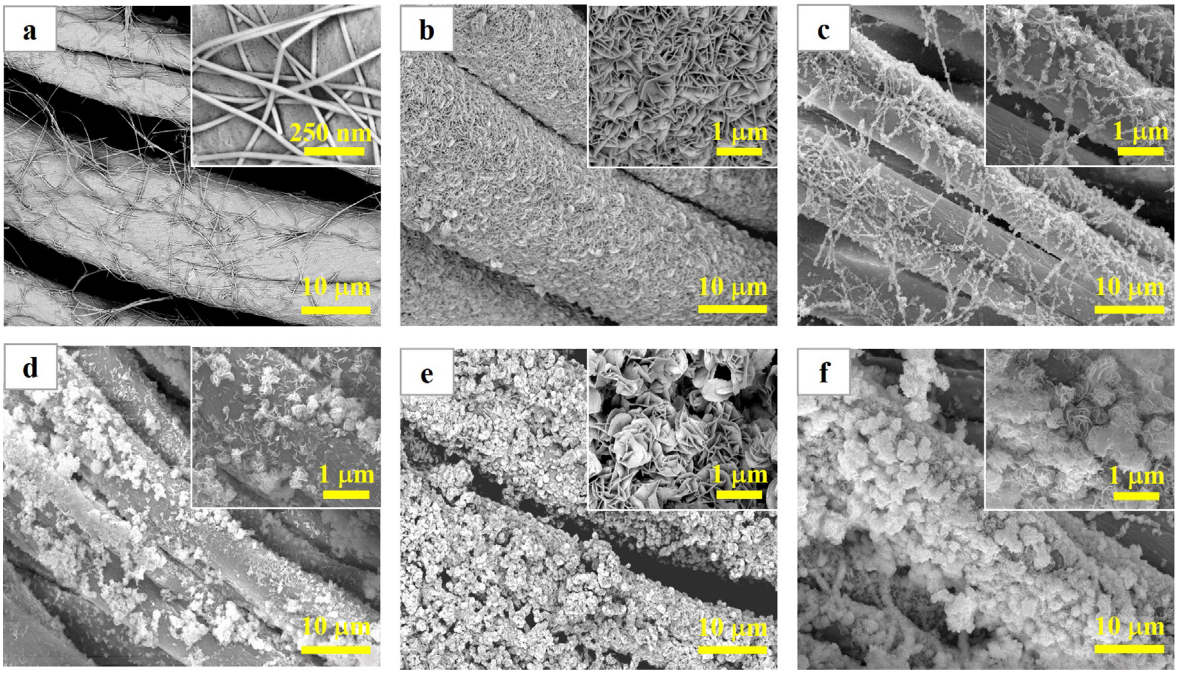

Fig. 3 SEM images: (a) AgNW/CF, (b) 9BiOBr/CF, (c) 3BiOBr/AgNW/CF, (d) 6BiOBr/AgNW/CF, (e) 9BiOBr/AgNW/CF, and (f) 12BiOBr/AgNW/CF. Insets in (a, b, c, d, e, and f) show the magnified surface morphology of the samples.

material (Johansson et al., 1999). The presence of element C in 9BiOBr/AgNW/CF is attributed to the existence of polysaccharides in cellulose. Fig. 5f also shows three peaks of C 1 s at 284.7 eV, 286.6 eV and 288.4 eV, corresponding to carbon atoms (C—C, C—OH and C═O) in different environments (Peng et al., 2013; Tian et al., 2019). The XRD, SEM, EDS and XPS analyses above confirms the successful fabrication of the targeted BiOBr/AgNW coated CF through our established process. The photocatalytic degradation performance and the corresponding mechanism of BiOBr/AgNW/CF are further explored in the following sections.

3.2. Photocatalytic study

3.2.1. Diffuse reflectance spectroscopy

The light absorption capacity determines the light utilization of photocatalyst. Thus, the sample was analyzed by UV–visible diffuse reflectance spectrum to demonstrate its light absorption range (Lin et al., 2012). As shown in Fig. 6a, the absorption edge of the BiOBr/AgNW/CF showed an obvious red shift compared with the 9BiOBr/CF, which is attributed to the existence of AgNW (Zhou et al., 2020). However, with the increase of SILAR cycles, the visible light response of the 12BiOBr/AgNW/CF display a modest increase, due to the light reflection occurred on the fiber surface.

The band gap value of the samples was obtained using the following theoretical equation (Wang et al., 2020): $\alpha h v = A(hv - Eg)^{(n/2)}$.

Where α, v, A, h, and Eg are the absorption coefficient, light frequency, constant, the Planck constant, and the band gap of the semiconductor, respectively. The n value of BiOBr is 4. Fig. 6b shows that the Eg values of 9BiOBr/CF and 9BiOBr/AgNW/CF, which are calculated as 2.96 and 2.84 eV. The band gap of photocatalytic composite 9BiOBr/AgNW/CF is reduced. In all, these results indicate that the combination of BiOBr and AgNW broadens the light absorbing range, which contributes to increasing the number of photo-generated carriers. Moreover, the band structure of BiOBr was estimated by VB-XPS and Mott-schottky curves, respectively. As shown in (Fig. S2a), the slope of Mott-schottky curves is positive, indicating that BiOBr is an *n*-type semiconductor (Wu et al., 2017). The flat band potential of BiOBr is 0.08 V vs Ag/AgCl, corresponding to 0.28 V vs NHE. The valance band top position of BiOBr is 1.79 eV below the E_f as shown in Fig. S2b. Combined with the E_g value, the VB and CB values of BiOBr are 2.07 eV and −0.77 eV, respectively, which demonstrates the ability to photo-reduce —OH to ·OH and oxidize O_2 to $\cdot O_2^-$.

3.2.2. Photoluminescence

Generally, a higher PL intensity represents a higher recombination efficiency of the electron-hole pairs, resulting in poor photocatalytic performance (Jiang et al., 2021). The PL spectrums of 9BiOBr/CF and BiOBr/AgNW/CF series are shown in Fig. 7. Obviously, the relative intensity of the emission peak of 9BiOBr/AgNW/CF is much lower than that of 9BiOBr/CF, which indicates that the recombination rate of photogenerated electrons and holes in 9BiOBr/AgNW/CF series is lower than that of 9BiOBr/CF, which indicates higher photocatalytic activity. Such result also indirectly demonstrates that there is an interaction between BiOBr and AgNW to promote the separation of electrons and holes in the catalyst.

3.2.3. Photocatalytic studies

In order to explore the photocatalytic effect of the composite catalyst under visible light, RhB was adopted as the example of residual dyestuff. As seen from Fig. 8a, the photocatalytic

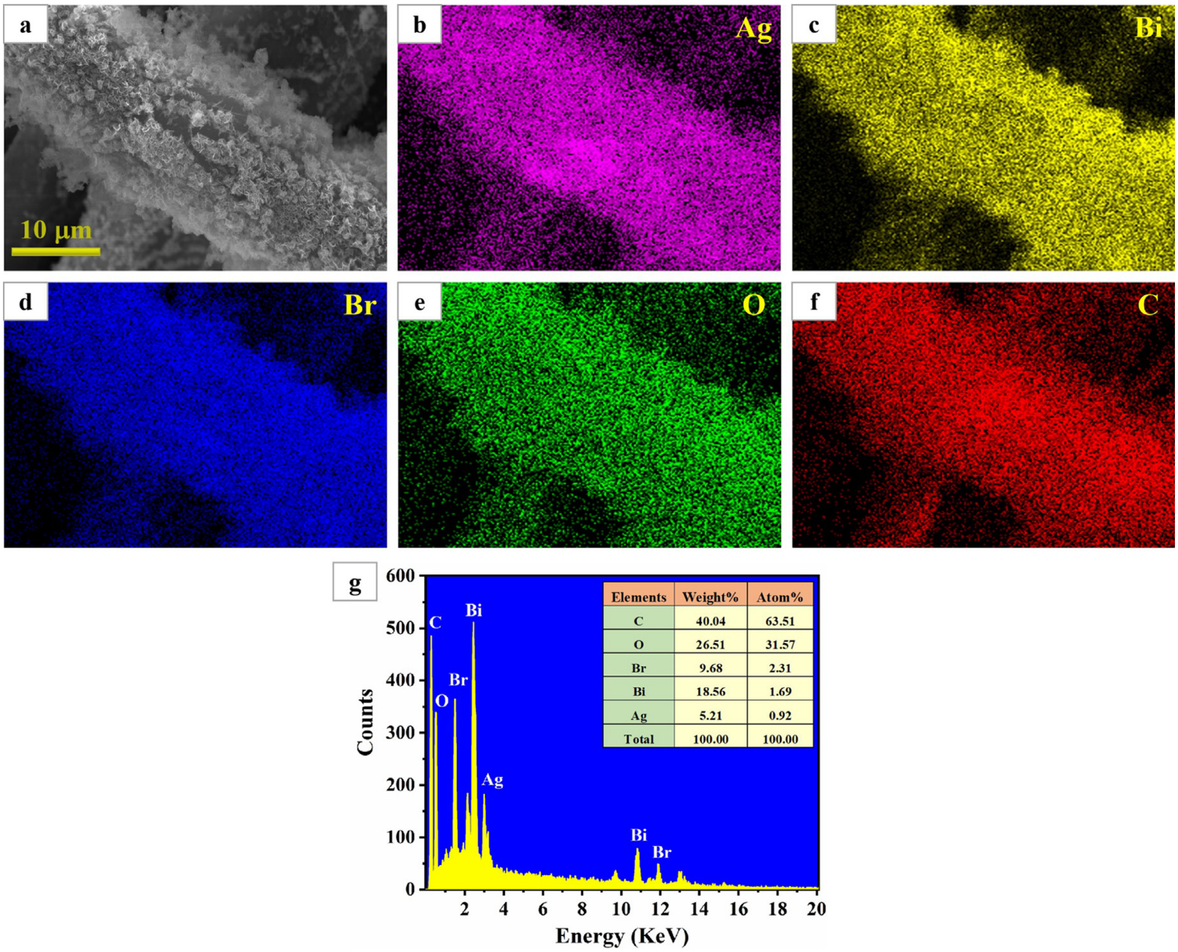

Elements	Weight%	Atom%
C	40.04	63.51
O	26.51	31.57
Br	9.68	2.31
Bi	18.56	1.69
Ag	5.21	0.92
Total	100.00	100.00

Fig. 4 (a–f) EDS mapping images and (g) EDS spectrum of 9BiOBr/AgNW/CF.

effect of BiOBr/AgNW/CF has been improved. The 9BiOBr/AgNW/CF displays best effect in the first 40 min with a degradation rate of 83 % for RhB.The degradation rate of RhB by 9BiOBr/CF is 56 %, but is still higher than that of BiOBr (Fig. S3). After 90 min, the degradation rate of RhB by 9BiOBr/AgNW/CF reaches 97 %, which is almost twice of that of commercial P25 (Fig. S3). This was due to the fact that AgNW aggregate electrons and enhance the separation of photogenerated electrons-holes, thus improving the photocatalytic performance. We also found that the effectiveness of the catalysts is improved with increasing number of cycles. 9BiOBrAgNW/CF also shows high photocatalytic activity for MO and MB, with a degradation rate above 70 % in 90 min (Fig. S4). However, the photocatalytic effect of 12BiOBr/AgNW/CF decreases, indicating that a proper number of SILAR cycle is conducive to achieving the balance of solar absorption and electron transport. Because of the large thickness of the BiOBr layer, the AgNW are affected by light. Thus, the electrons are unable to vibrate to the surface, which leads to the decrease of photocatalytic efficiency.

Then we further studied the rate of RhB degradation by the catalyst and fitted the kinetic equation. The results are shown in Fig. 8b. It is obvious that the reaction is obeyed with the first-order kinetic equation: $\ln(C_0/C) = kt$.

Where t represents the reaction time, C_0 represents the initial concentration, C represents the concentration corresponding to each reaction time, and k is the reaction rate constant (Zhou et al., 2019). The results showed that the constant k for 9BiOBr/AgNW/CF is 0.0377 min^{-1}, which is approximately 4.5, 2.9, 1.4, and 2.2 times larger than that of 9BiOBr/CF, 3BiOBr/AgNW/CF, 6BiOBr/AgNW/CF and 12BiOBr/AgNW/CF, respectively. This result further verifies that the photocatalytic effect of 9BiOBr/AgNW/CF is the best, which is consistent with the results of UV–visible diffuse reflectance and photoluminescence spectra. In addition, the reaction rate constant of the 9BiOBr/AgNW/CF in this study ($k = 0.0377\ \text{min}^{-1}$) is significantly larger than the similar experiment conducted by Li ($k_{\text{Ag/BiOBr/GO}} = 0.0277\ \text{min}^{-1}$) (Li et al., 2020), Zhang ($k_{\text{P25}} = 0.0003\ \text{min}^{-1}$, $k_{\text{BiOBr}} = 0.0033\ \text{min}^{-1}$, $k_{40\%\text{BiOCl/BiOBr}} = 0.0068\ \text{min}^{-1}$) (Zhang et al., 2018), Cai ($k_{\text{BiOBr}} = 0.008\ \text{min}^{-1}$, $k_{\text{BiOBr@TiO2-6}} = 0.025\ \text{min}^{-1}$) (Cai et al., 2018), Guo ($k_{\text{Ag/CDots/BiOBr}} = 0.0055\ \text{min}^{-1}$) (Guo et al., 2018), and Tang ($k_{\text{CoS/BiOBr}} = 0.0074\ \text{min}^{-1}$) (Tang et al., 2021). Fig. S5 shows the nitrogen adsorption–desorption isotherms of BiOBr and 9BiOBr/AgNW/CF. All the isotherms curves exhibited type IV with a type H3 hysteresis loops, which showed that mesopores were formed in the samples. The BET specific surface areas of the BiOBr and 9BiOBr/AgNW/CF are 5.74 m^2/g and 4.33 m^2/g, respectively. While the BJH adsorption average pore diameters of the BiOBr and 9BiOBr/AgNW/CF are 21.46 nm and 53.68 nm, respectively, which indicate that the CF substrates can support BiOBr nanosheets and

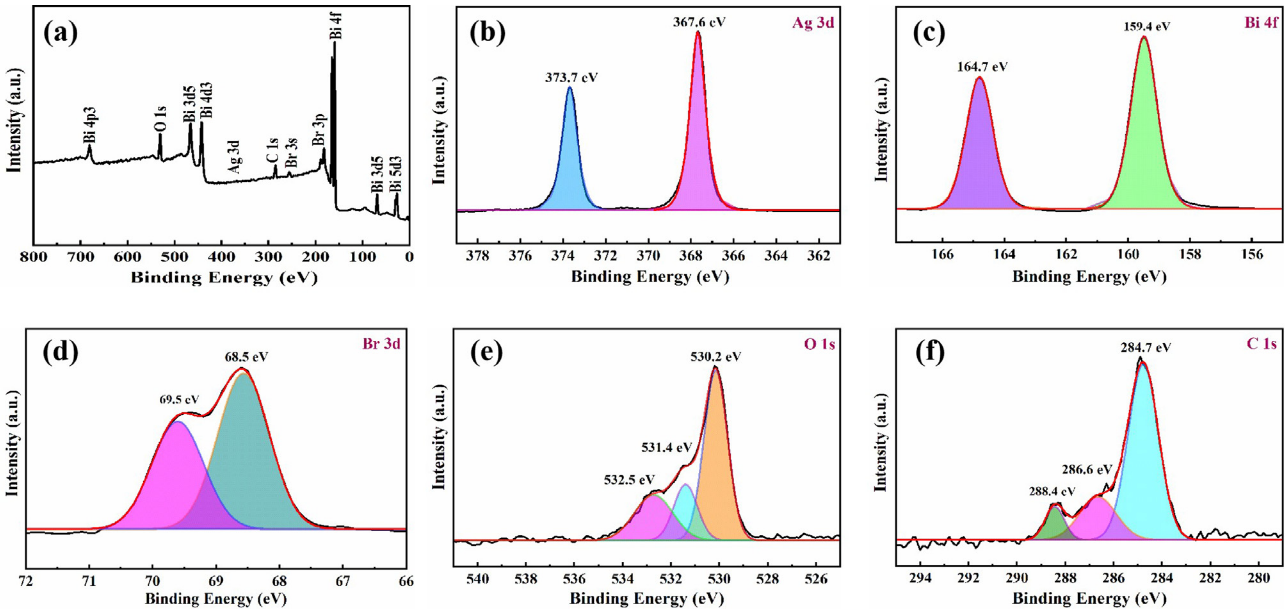

Fig. 5 XPS spectra of 9BiOBr/AgNW/CF: (a) full spectrum, (b) Ag 3d, (c) Bi 4f, (d) Br 3d, (e) O 1 s, and (f) C 1 s.

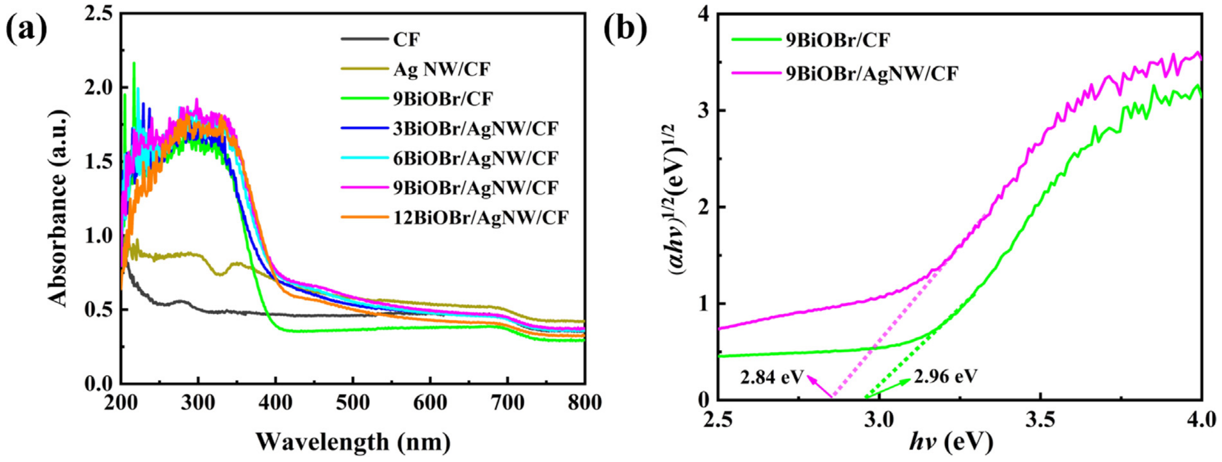

Fig. 6 (a) UV–vis absorption spectra and (b) Kubelka–Munk plots.

effectively reduce the aggregation of photocatalysts. Furthermore, the catalytic activity of 9BiOBr/AgNW/CF was higher than that of BiOBr (Fig. S3), indicating that S_{BET} was not the only factor influencing photocatalytic activity.

The separation efficiency of photogenerated e^- and h^+ pairs is evaluated by the photocurrent transient response of the photocatalysts (Jiang et al., 2016). As shown in Fig. S6a, the photocurrent intensity of the BiOBr/AgNW/CF series is significantly higher than that of BiOBr/CF, suggesting that more effective interfacial charges are separated between BiOBr and AgNW. Besides, the electrochemical impedance spectroscopy (EIS) was examined to further gain insight into the charge-transfer behavior. The EIS spectra (Fig. S6b) exhibit that 9BiOBr/AgNW/CF has a smaller arc radius than that of 9BiOBr/CF or 9BiOBr/AgNW/CF series, which indicates that it has higher photo-generated charge separation and transfer efficiency (Di et al., 2016). This result is also consistent with the photocatalytic performance, PL and photocurrent response.

In addition, we also studied the recyclability and photocatalytic stability of 9BiOBr/AgNW/CF (Fig. 8c). After five cyclic degradation experiments, the degradation rate of the sample decreased from 97 % to 89 %. The degradation rate decreased by less than 10 %, indicating that the prepared BiOBr/AgNW/CF had good stability and reusability. The slight decline in photocatalytic performance is attributed to the loss of some photocatalysts or the unwashed of some simulated dyes occupying the active sites of the photocatalysts in each process of recovering the catalytic materials, resulting in a decrease in their degradation rate. As seen from Fig. S7, no obvious morphological change or no new diffraction peaks is observed after five times of reuse, which further demonstrates the stability of the photocatalyst.

In order to further study the mineralization rate of RhB, total organic carbon (TOC) is determined (Fig. 8d). The results of TOC removal are consistent with decoloration results. However, the removal efficiency of TOC is lower than that of degra-

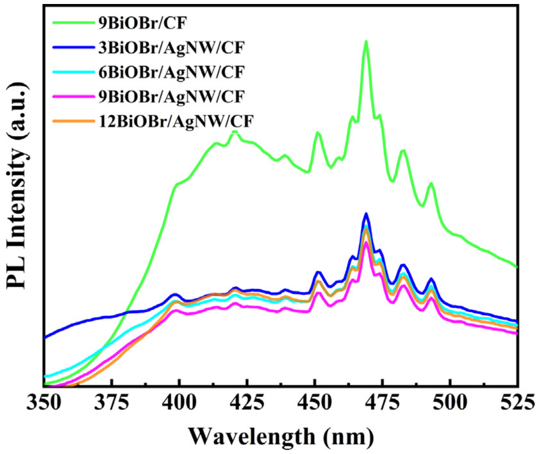

Fig. 7 PL spectra of 9BiOB/CF and the BiOBr/AgNW/CF series under sunlight irradiation.

dation, indicating that mineralization is incomplete. This is because the decolorization of dyes reduces the absorbance. However, in the process of photocatalytic degradation, RhB was first degraded into intermediates, and then mineralized into CO_2 and H_2O.

3.2.4. Mechanism of enhancement of photocatalytic activity

In order to further explore the photocatalytic mechanism of the composite catalyst, we carried out the active species capturing experiments. The tests were conducted in a same condition aforementioned except benzoquinone (BQ), tert-butanol (TBA) and disodium ethylenediamine tetraacetate (EDTA-2Na) were added to trap superoxide free radical ($\bullet O_2^-$), hydroxyl radical (•OH), and holes (h^+), respectively (Jiang et al., 2021; Peper et al., 2017). According to the degradation rate of RhB under visible light irradiation, we can judge the role of various active species in the photocatalytic degradation reaction. The capture test results are shown in Fig. 9a. The degradation rate of 9BiOBr/AgNW/CF to RhB was 97 % after 90 min without trapping agents. After adding EDTA-2Na, the photocatalytic activity of 9BiOBr/AgNW/CF is greatly inhibited. The degradation rate is only 29.6 %, indicating that h^+ is the main active species in this reaction. Moreover, the degradation rate is 73.1 % upon the addition of BQ into the system, indicating that •OH plays a very important role in this reaction. Contrarily, after adding TBA, the degradation rate of 9BiOBr/AgNW/CF to RhB is up to 92.4 %, and the change of degradation rate was small, indicating that $\bullet O_2^-$ plays a negligible role in the reaction.

After that, the active free radicals produced by 9BiOBr/AgNW/CF composites under sunlight are further confirmed by ESR technique (Fig. 9b). Both DMPO- $\bullet O_2^-$ and DMPO-•OH show typical peaks after irradiation for 5 min. No electron spin resonance signal is found in the dark, which indicates that the results of ESR are consistent with that obtained in the free radical trapping experiment. By contrast, both DMPO-$\bullet O_2^-$ and DMPO- •OH signals are detected in terms of 9BiOBr/CF under visible light in Fig. S8, which is evidence of the formation of $\bullet O_2^-$ and •OH radicals during the photocat-

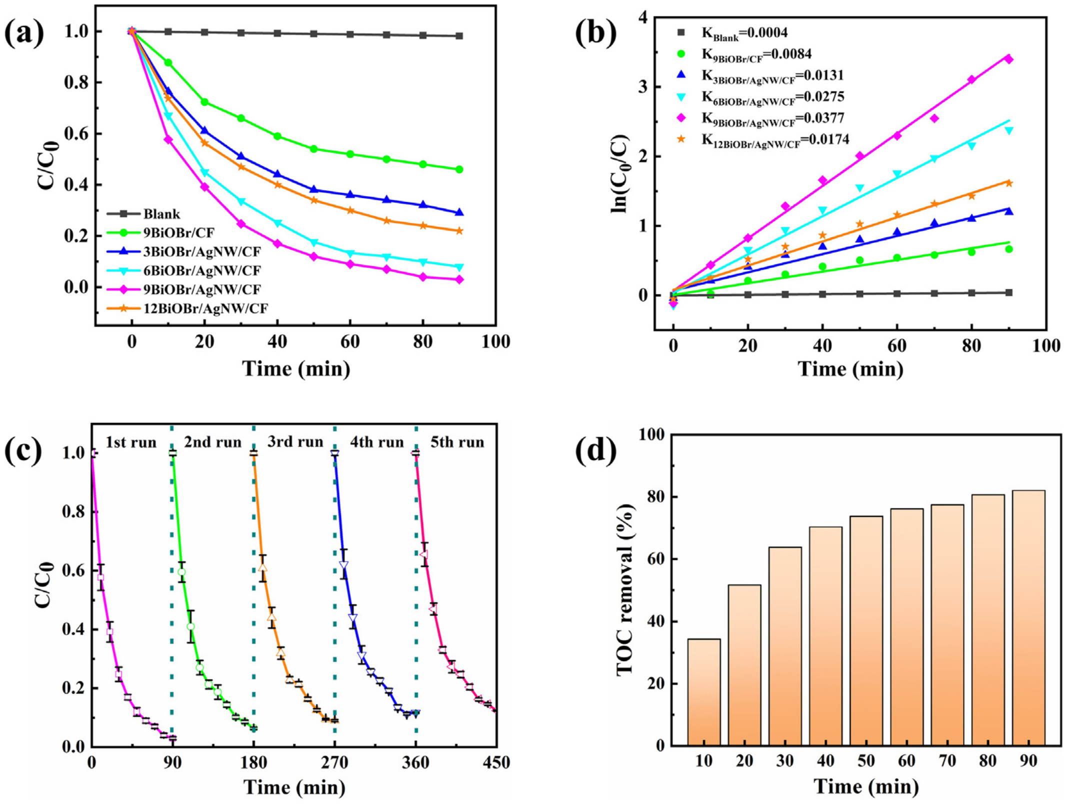

Fig. 8 (a) Photocatalytic activities, (b) kinetics of samples for the degradation of RhB under visible light irradiation, (c) cyclic performance of 9BiOBr/AgNW/CF, and (d) TOC changes during the course of RhB photodecomposition.

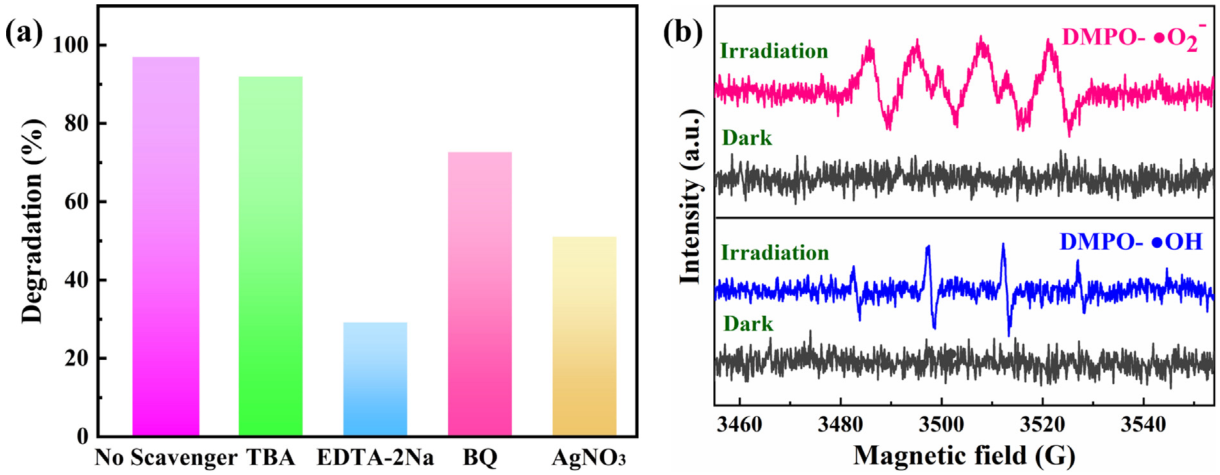

Fig. 9 (a) Photocatalytic degradation of RhB in visible light with different scavengers, (b) ESR spectra of 9BiOBr/AgNW/CF in the methanol dispersion for DMPO-$\bullet O_2^-$ and aqueous dispersion for DMPO-$\bullet$OH.

alytic reaction. However, 9BiOBr/CF shows lower signal intensity than that of 9BiOBr/AgNW/CF, indicating the photo-redox ability is enhanced by the introduction of AgNW.

On this basis, a possible photocatalytic degradation mechanism is proposed. The mechanism process is shown in Fig. 10. Under the irradiation of visible light, the electron is excited by a specific wavelength of light, and transits from the valence band of BiOBr to the conduction band. At the same time, a positively charged hole is left in the valence band. The photogenerated electrons migrates to the AgNW and gathers on the Ag nanowires. The O_2 adsorbed on the surface of the catalyst reacts with the electrons on the AgNW to form $\bullet O_2^-$, to oxidize the RhB. Due to the aggregation of electrons by AgNW, the separation of electrons and holes is enhanced, so that more holes in the valence band directly react with the RhB adsorbed on the surface of the catalyst. The photocatalytic reaction mechanism for the degradation of RhB using BiOBr/AgNW/CF is described as follows,

$$\text{BiOBr} + h\nu\ (\text{visible light}) \rightarrow \text{BiOBr}\ (e^- + h^+) \tag{1}$$

$$e^- + \text{Ag} \rightarrow \text{Ag}(e^-) \tag{2}$$

$$\text{Ag}\ (e^-) + O_2 \rightarrow \bullet O_2^- \tag{3}$$

$$\bullet O_2^- + H^+ \rightarrow \bullet OOH \rightarrow \bullet OH \tag{4}$$

$$h^+ + H_2O \rightarrow \bullet OH + H^+ \tag{5}$$

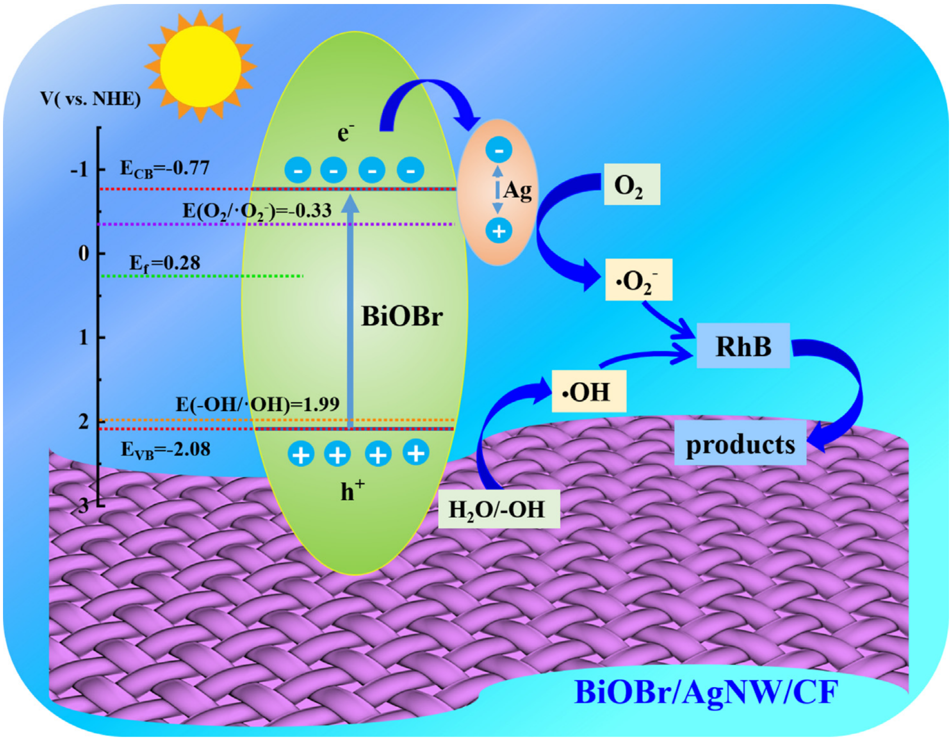

Fig. 10 Mechanism of photocatalytic degradation of RhB under visible light irradiation.

$$OH^- + h^+ \rightarrow \bullet OH \quad (6)$$

$$\text{Active species } (h^+, \bullet OH, \text{ and } \bullet O_2^-) + \text{pollutants} \rightarrow \text{degradationproducts.} \quad (7)$$

To further explore the possible degradation pathway of RhB over BiOBr/AgNW/CF, intermediates were detected to investigate the degradation mechanism. On the basis of the intermediates obtained from the mass spectra (Fig. S9), the possible degradation pathway of RhB is proposed. Fig. S9a depicts the mass spectrum of RhB solution without light illumination. The strong peak at the strong peak at m/z 443.2 is the ion peak of RhB molecules. As shown in Fig. S9b, the presence of two products with m/z 415.2 and 387.2 are the ion peaks of RhB molecules after removing one and two ethyl groups, respectively. After visible light irradiation for 60 min (Fig. S9c), the new peak at 359.2 and 491.3 belongs to the ion peak of RhB molecules after removing three ethyl groups and the intermediate formed by hydroxylation of RhB molecules by three •OH, respectively. The new peak at *m/z* 318.3 is attributed to RhB intermediate products generated by the hydroxylation of two diethylamine fragments and one •OH, while the peak at 274.2 is produced from the substance after the intermediates have been decarboxylated. The peaks are observed at 230 and 126 due to the lone bond attacked by •OH between the top and lower conjugated structures in RhB molecules. Therefore, the deethylation and hydroxylation process are the important stages during the degradation treatment. Meanwhile, the conjugated structure of RhB molecules is successively fragmented into small molecules, which are finally oxidized into CO_2 and H_2O (Zhang et al., 2020).

4. Conclusions

In summary, we prepared BiOBr/AgNW/CF photocatalytic composites which were easy to be recycled by simple impregnation and SILAR methods. AgNW provides a faster charge transfer channel in BiOBr/AgNW/CF catalytic materials compared with BiOBR/CF, thus significantly improves the photocatalytic performance. Furthermore, the photocatalytic activity of BiOBr/AgNW/CF is relatively stable due to the fact that AgNW is not easily oxidized by air under the protection of BiOBr. The improvement of these properties show that BiOBr/AgNW/CF photocatalytic composites have great application potential in dye degradation, water treatment and general environmental applications.

Acknowledgments

This work is financially supported by the research funding from Yancheng Institute of Technology (xjr2020009), the National Natural Science Foundation of China (52103067), and the Natural Science Foundation of Jiangsu Province (BK 20191045).

Appendix A. Supplementary material

Supplementary data to this article can be found online at https://doi.org/10.1016/j.arabjc.2023.104624.

References

Akhundi, A., Habibi-Yangjeh, A., Abitorabi, M., et al, 2019. Review on photocatalytic conversion of carbon dioxide to value-added compounds and renewable fuels by graphitic carbon nitride-based photocatalysts. Catal. Rev. 61 (4), 595–628.

Akhundi, A., Badiei, A., Ziarani, G.M., et al, 2020. Graphitic carbon nitride-based photocatalysts: toward efficient organic transformation for value-added chemicals production. Mol. Catal. 488, 110902.

Akhundi, A., Zaker Moshfegh, A., Habibi-Yangjeh, A., et al, 2022. Simultaneous dual-functional photocatalysis by g-C_3N_4-based nanostructures. ACS ES&T Eng. 2 (4), 564–585.

Bhatia, D., Sharma, N., Singh, J., et al, 2017. Biological methods for textile dye removal from wastewater: A review. Crit. Rev. Environ. Sci. Technol. 47 (19), 1836–1876.

Bustos-Terrones, Y., Hermosillo-Nevárez, J., Ramírez-Pereda, B., et al, 2021. Removal of BB9 textile dye by biological, physical, chemical, and electrochemical treatments. J. Taiwan Inst. Chem. E 121, 29–37.

Cai, Y., Song, J., Liu, X., et al, 2018. Soft BiOBr@TiO_2 nanofibrous membranes with hierarchical heterostructures as efficient and recyclable visible-light photocatalysts. Environ. Sci.: Nano 5 (11), 2631–2640.

Celebioglu, A., Topuz, F., Yildiz, Z.I., et al, 2019. One-step green synthesis of antibacterial silver nanoparticles embedded in electrospun cyclodextrin nanofibers. Carbohyd. Polym. 207, 471–479.

Chairungsri, W., Subkomkaew, A., Kijjanapanich, P., et al, 2022. Direct dye wastewater photocatalysis using immobilized titanium dioxide on fixed substrate. Chemosphere 286, 131762.

Cheon, S., Kang, H., Kim, H., et al, 2018. High-performance triboelectric nanogenerators based on electrospun polyvinylidene fluoride-silver nanowire composite nanofibers. Adv. Funct. Mater. 28 (2), 1703778.

Chimupala, Y., Phromma, C., Yimklan, S., et al, 2020. Dye wastewater treatment enabled by piezo-enhanced photocatalysis of single-component ZnO nanoparticles. RSC Adv. 10 (48), 28567–28575.

Di, J., Xia, J., Ji, M., et al, 2016. Advanced photocatalytic performance of graphene-like BN modified BiOBr flower-like materials for the removal of pollutants and mechanism insight. Appl. Catal B 183, 254–262.

Gao, D., Li, Y., Lyu, B., et al, 2019. Construction of durable antibacterial and anti-mildew cotton fabric based on P (DMDAAC-AGE)/Ag/ZnO composites. Carbohyd. Polym. 204, 161–169.

Geng, Y., Li, N., Ma, J., et al, 2017. Preparation, characterization and photocatalytic properties of BiOBr/ZnO composites. J. Energy Chem. 26 (3), 416–421.

Guo, J., Yan, D.Y., Lam, F.L., et al, 2019. Self-cleaning BiOBr/Ag photocatalytic membrane for membrane regeneration under visible light in membrane distillation. Chem. Eng. J. 378, 122137.

Guo, Y., Zhang, J., Zhou, D., et al, 2018. Fabrication of Ag/CDots/BiOBr ternary photocatalyst with enhanced visible-light driven photocatalytic activity for 4-chlorophenol degradation. J. Mol. Liq. 262, 194–203.

Hou, R., Gao, Y., Zhu, H., et al, 2017. Coupling system of Ag/BiOBr photocatalysis and direct contact membrane distillation for complete purification of N-containing dye wastewater. Chem. Eng. J. 317, 386–393.

Ishak, S., Murshed, M., Md, A.H., et al, 2020. The application of modified natural polymers in toxicant dye compounds wastewater: a review. Water 12 (7), 2032.

Jiang, D., Du, X., Chen, D., et al, 2016. Facile wet chemical method for fabricating p-type BiOBr/n-type nitrogen doped graphene composites: efficient visible-excited charge separation, and high-performance photoelectrochemical sensing. Carbon 102, 10–17.

Jiang, P., Yu, K., Yuan, H., et al, 2021. Encapsulating Ag nanoparticles into ZIF-8 as an efficient strategy to boost uranium photoreduction without sacrificial agents. J. Mater. Chem. A 9 (15), 9809–9814.

Johansson, L., Campbell, J.M., Koljonen, K., et al, 1999. Evaluation of surface lignin on cellulose fibers with XPS. Appl. Surf. Sci. 144, 92–95.

Li, K., Gong, K., Liu, J., et al, 2021. New insights into the role of sulfite in BiOX photocatalytic pollutants elimination: In-operando generation of plasmonic Bi metal and oxygen vacancies. J. Hazard. Mater. 418, 126207.

Li, W., Mu, B., Yang, Y., 2019. Feasibility of industrial-scale treatment of dye wastewater via bio-adsorption technology. Bioresource Technol. 277, 157–170.

Li, C., Wang, B., Zhang, F., et al, 2020. Performance of Ag/BiOBr/GO composite photocatalyst for visible-light-driven dye pollutants degradation. J. Mater. Res. Technol. 9 (1), 610–621.

Lin, H., Cao, J., Luo, B., et al, 2012. Visible-light photocatalytic activity and mechanism of novel AgBr/BiOBr prepared by deposition-precipitation. Chin. Sci. Bull. 57 (22), 2901–2907.

Ling, Y., Dai, Y., Zhou, J., 2020. Fabrication and high photoelectrocatalytic activity of scaly BiOBr nanosheet arrays. J. Colloid Interf. Sci. 578, 326–337.

Liu, L., Chen, Z., Zhang, J., et al, 2021. Treatment of industrial dye wastewater and pharmaceutical residue wastewater by advanced oxidation processes and its combination with nanocatalysts: a review. J. Water Process Eng. 42, 102122.

Lv, X., Yan, D.Y., Lam, F.L., et al, 2020. Solvothermal synthesis of copper-doped BiOBr microflowers with enhanced adsorption and visible-light driven photocatalytic degradation of norfloxacin. Chem. Eng. J. 401, 126012.

Meerbergen, K., Crauwels, S., Willems, K., et al, 2017. Decolorization of reactive azo dyes using a sequential chemical and activated sludge treatment. J. Biosci. Bioeng. 124 (6), 668–673.

Miao, Y., Lian, Z., Huo, Y., et al, 2018. Microwave-assisted ionothermal synthesis of hierarchical microcube-like BiOBr with enhanced photocatalytic activity. Chinese J. Catal. 39 (8), 1411–1417.

Noureen, L., Xie, Z., Gao, Y., et al, 2020. Multifunctional Ag_3PO_4-rGO-coated textiles for clean water production by solar-driven evaporation, photocatalysis, and disinfection. ACS Appl. Mater. Inter. 12 (5), 6343–6350.

Peng, S., Li, L., Tan, H., et al, 2013. Monodispersed Ag nanoparticles loaded on the PVP-assisted synthetic $Bi_2O_2CO_3$ microspheres with enhanced photocatalytic and supercapacitive performances. J. Mater. Chem. A 1 (26), 7630–7638.

Peper, J.L., Vinyard, D.J., Brudvig, G.W., et al, 2017. Slow equilibration between spectroscopically distinct trap states in reduced TiO_2 nanoparticles. J. Am. Chem. Soc. 139 (8), 2868–2871.

Piaskowski, K., Świderska-Dąbrowska, R., Zarzycki, P.K., 2018. Dye removal from water and wastewater using various physical, chemical, and biological processes. J. Aoac. Int. 101 (5), 1371–1384.

Ratnayake, S.P., Ren, J., Colusso, E., et al, 2021. SILAR deposition of metal oxide nanostructured films. Small 17 (49), 2101666.

Sabri, M., Habibi-Yangjeh, A., Rahim, P.S., et al, 2021. Titania-activated persulfate for environmental remediation: the-state-of-the-art. Catal. Rev., 1–56

Shi, X., Wang, P., Li, W., et al, 2019. Change in photocatalytic NO removal mechanisms of ultrathin BiOBr/BiOI via NO_3-adsorption. Appl. Catal. B: Environ. 243, 322–329.

Shi, Z., Zhang, Y., Liu, T., et al, 2020. Synthesis of BiOBr/Ag_3PO4 heterojunctions on carbon-fiber cloth as filter-membrane-shaped photocatalyst for treating the flowing antibiotic wastewater. J. Colloid Interf. Sci. 575, 183–193.

Slama, H., Chenari, B.A., Pourhassan, Z., et al, 2021. Diversity of synthetic dyes from textile industries, discharge impacts and treatment methods. Appl. Sci. 11 (14), 6255.

Srivatsav, P., Bhargav, B., Shanmugasundaram, V., et al, 2020. Biochar as an eco-friendly and economical adsorbent for the removal of colorants (dyes) from aqueous environment: a review. Water 12 (12), 3561.

Tang, Q., Yang, M., Yang, S., et al, 2021. Enhanced photocatalytic degradation of glyphosate over 2D CoS/BiOBr heterojunctions under visible light irradiation. J. Hazard. Mater. 407, 124798.

Tian, C., Luo, S., She, J., et al, 2019. Cellulose nanofibrils enable flower-like BiOCl for high-performance photocatalysis under visible-light irradiation. Appl. Surf. Sci. 464, 606–615.

Tkaczyk, A., Mitrowska, K., Posyniak, A., 2020. Synthetic organic dyes as contaminants of the aquatic environment and their implications for ecosystems: a review. Sci. Total Environ. 717, 137222.

Uddin, F., 2021. Environmental hazard in textile dyeing wastewater from local textile industry. Cellulose 28 (17), 10715–10739.

Wang, W., Liang, T., Bai, H., et al, 2018. All cellulose composites based on cellulose diacetate and nanofibrillated cellulose prepared by alkali treatment. Carbohyd. Polym. 179, 297–304.

Wang, S., Ma, W., Fang, Y., et al, 2014. Bismuth oxybromide promoted detoxification of cylindrospermopsin under UV and visible light illumination. Appl. Catal. B: Environ. 150, 380–388.

Wang, L., Mao, H., Li, Z., et al, 2020. Immobilizing Ag/Cu_2O on cotton fabric to enhance visible light photocatalytic activity. New J. Chem. 44 (47), 20759–20769.

Wang, L., Wang, J., Tang, M., et al, 2023. Developing a Z-scheme Ag_2CO_3/ZIF-8 heterojunction for the surface decoration of cotton fabric toward repeatable photocatalytic dye degradation. Appl. Surf. Sci. 610, 155605.

Weng, C., Wang, G., Dai, Z., et al, 2019. Buckled AgNW/MXene hybrid hierarchical sponges for high-performance electromagnetic interference shielding. Nanoscale 11 (47), 22804–22812.

Wu, X., Ng, Y.H., Wang, L., et al, 2017. Improving the photo-oxidative capability of BiOBr via crystal facet engineering. J. Mater. Chem. A 5 (17), 8117–8124.

Wu, D., Yue, S., Wang, W., et al, 2016. Boron doped BiOBr nanosheets with enhanced photocatalytic inactivation of *Escherichia coli*. Appl. Catal. B 192, 35–45.

Xu, D., Ma, H., 2021. Degradation of rhodamine B in water by ultrasound-assisted TiO_2 photocatalysis. J. Clean. Prod. 313, 127758.

Yang, F., Sheng, B., Wang, Z., et al, 2021. Performance of UV/acetylacetone process for saline dye wastewater treatment: kinetics and mechanism. J. Hazard. Mater. 406, 124774.

Yang, Y., Zhang, C., Lai, C., et al, 2018. BiOX (X = Cl, Br, I) photocatalytic nanomaterials: applications for fuels and environmental management. Adv. Colloid Interfac. 254, 76–93.

Yu, Q., Chen, J., Li, Y., et al, 2020. In-situ decoration of metallic Bi on BiOBr with exposed (1 1 0) facets and surface oxygen vacancy for enhanced solar light photocatalytic degradation of gaseous n-hexane. Chinese J. Catal. 41 (10), 1603–1612.

Zhang, R., Han, Q., Li, Y., et al, 2020. Solvothermal synthesis of a peony flower-like dual Z-scheme PANI/BiOBr/$ZnFe_2O_4$ photocatalyst with excellent photocatalytic redox activity for organic pollutant under visible-light. Sep. Purif. Technol. 234, 116098.

Zhang, J., Wang, Y., Zhang, L., et al, 2014. Understanding changes in cellulose crystalline structure of lignocellulosic biomass during ionic liquid pretreatment by XRD. Bioresource Technol. 151, 402–405.

Zhang, J., Lv, J., Dai, K., et al, 2018. One-step growth of nanosheet-assembled BiOCl/BiOBr microspheres for highly efficient visible photocatalytic performance. Appl. Surf. Sci. 430, 639–646.

Zhou, W., Sun, S., Jiang, Y., et al, 2019. Template in situ synthesis of flower-like BiOBr/microcrystalline cellulose composites with highly visible-light photocatalytic activity. Cellulose 26 (18), 9529–9541.

Zhou, P., Zhang, L., Dai, Y., et al, 2020. Construction of a metallic silver nanoparticle-decorated bismuth oxybromide-based composite material as a readily recyclable photocatalyst. J. Clean. Prod. 246, 119007.

Zhu, W., Wang, P., Chen, Z., et al, 2022. A one-pot self-assembled AgNW aerogel electrode with ultra-high electric conductivity for intrinsically 500% super-stretchable high-performance Zn–Ag batteries. J. Mater. Chem. A 10, 10780–10789.